ACS APPLIED MATERIALS & INTERFACES

Research Article

www.acsami.org

Nanosheets of Earth-Abundant Jarosite as Novel Anodes for High-Rate and Long-Life Lithium-Ion Batteries

Yuan-Li Ding,[‡] Yuren Wen,[§] Chia-Chin Chen,[‡] Peter A. van Aken,[§] Joachim Maier,[‡] and Yan Yu*[,†,‡]

[†]Key Laboratory of Materials for Energy Conversion, Chinese Academy of Sciences, Department of Materials Science and Engineering, University of Science and Technology of China, Hefei, 230026 Anhui, PR China

[‡]Max Planck Institute for Solid State Research, Heisenbergstrasse 1, 70569 Stuttgart, Germany

[§]Max Planck Institute for Intelligent Systems, Heisenbergstrasse 3, 70569 Stuttgart, Germany

Supporting Information

ABSTRACT: Nanosheets of earth-abundant jarosite were fabricated via a facile template-engaged redox coprecipitation strategy at room temperature and employed as novel anode materials for lithium-ion batteries (LIBs) for the first time. These 2D materials exhibit high capacities, excellent rate capability, and prolonged cycling performance. As for $KFe_3(SO_4)_2(OH)_6$ jarosite nanosheets (KNSs), the reversible capacities of above 1300 mAh g^{-1} at 100 mA g^{-1} and 620 mAh g^{-1} after 4000 cycles at a very high current density of 10 A g^{-1} were achieved, respectively. Moreover, the resulting 2D nanomaterials retain good structural integrity upon cycling. These results reveal great potential of jarosite nanosheets as low-cost and high-performance anode materials for next-generation LIBs.

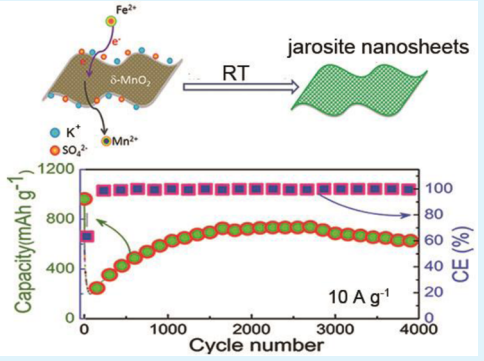

KEYWORDS: *lithium-ion batteries, jarosite, nanosheets, 2D, redox coprecipitation*

1. INTRODUCTION

Rechargeable lithium-ion batteries (LIBs) have empowered consumer electronics and are now considered as the best choice to propel forward the development of eco-friendly hybrid electric vehicles (HEVs) and electric vehicles (EVs).[1,2] This drives researchers and engineers to build better LIBs by optimizing several aspects including the energy density, rate capability, economy, safety, and sustainability. To achieve this goal, there has been an intensive search for new materials with high capacity, low cost, and environmental benignity for use as cathode or anode materials.[1,3−5] In the case of anode materials, many possible alternatives to carbonaceous materials, such as Fe-,[6,7] Mn-,[8] Sn-,[9,10] Si-,[11,12] and P-based materials,[13] have been developed owing to their low cost, earth-abundance, and nontoxicity together with high theoretical capacities of 900−4000 mAh g^{-1}, more than 2−10 times higher than that of commercial graphite (370 mAh g^{-1}). Among them, Fe-based compounds are more attractive considering that iron is the fourth most abundant element in the earth's crust. Moreover, the effective synthesis of Fe-based materials is relatively easy to be achieved in most cases. For that reason, a great effort is being directed toward the development of Fe-based materials, such as Fe_2O_3,[14] Fe_3O_4,[15] FeS,[6] Fe_3C,[16] FeP,[17,18] and ferrites (MFe_2O_4, M═Zn, Cu, and Cd).[19−22] Compared with these compounds, Fe-based polyanionic compounds,[23,24] such as jarosite, might be even more attractive because of their relatively high stability in acidic environments and facile fabrication.[25,26]

Jarosite is an earth-abundant natural mineral in acidic and sulfate-rich environment.[26,27] As shown in Figure 1a, the crystals are rhombohedral and of *R*3-*m* symmetry with lattice constants $a = b = 7.30$ Å and $c = 17.09$ Å at room temperature.[28] Jarosite $KFe_3(SO_4)_2(OH)_6$ (K-jarosite) is an ideal kagome lattice compound, and has been studied extensively for its spin chirality on a two-dimensional (2D) geometrically frustrated lattice and unique magnetic properties.[29] In this work, we investigate Li-storage behaviors of K-jarosite and its analogue $[NaFe_3(SO_4)_2(OH)_6]$ (Na-jarosite) at a voltage range of 0.005−3.0 V and demonstrate their great potential as a new class of anode materials for high-performance LIBs.

Meanwhile, in addition to the advantages of nanosized materials in facilitating fast Li^+/electron transport because of the increased surface areas and the shortened ion diffusion distance,[30] 2D nanomaterials are particularly attractive because a large fraction of atoms on the surface offer sufficient active contacts. Although an ultrasmall thickness is beneficial to fast Li^+ insertion/extraction, lateral submicrometric or micrometric dimensions can keep structural integrity and effectively accommodate the volume changes because of repeated Li^+ insertion/extraction, leading to better cycling stability. From this point of view, there has been substantial research effort to

Received: March 9, 2015
Accepted: April 27, 2015
Published: April 27, 2015

DOI: 10.1021/acsami.5b01992
ACS Appl. Mater. Interfaces 2015, 7, 10518−10524

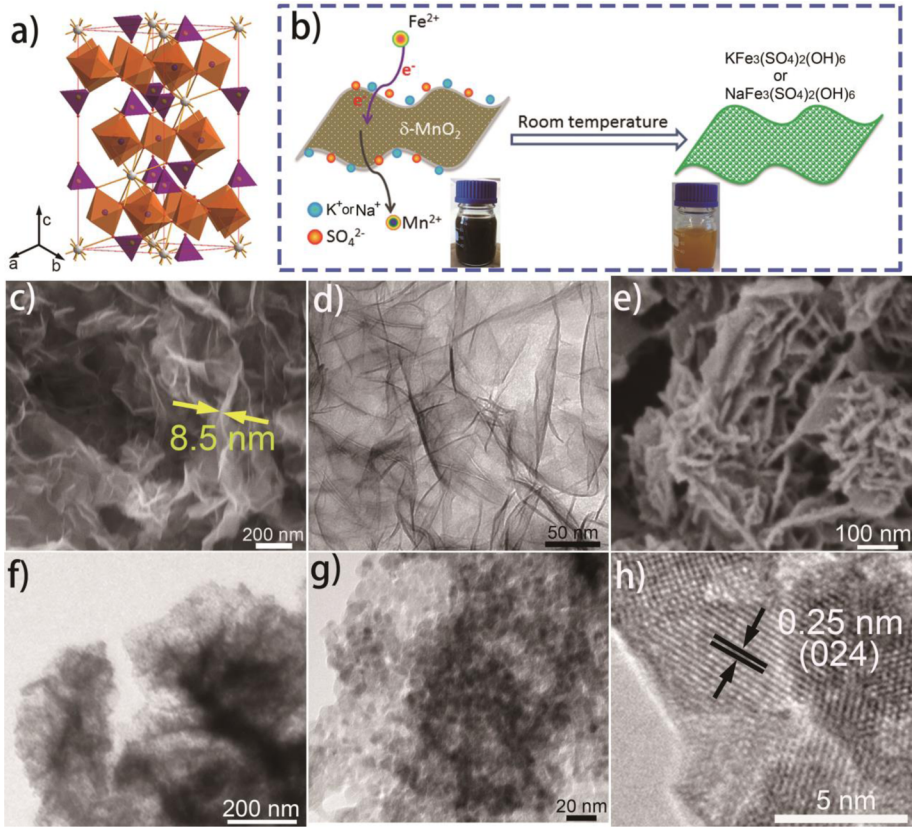

Figure 1. (a) Crystal structure of $KFe_3(SO_4)_2(OH)_6$. Hydrogen atoms are omitted for clarity. FeO_6, octahedra; SO_4, tetrahedra; K, Fe, S, and O atoms are displayed in orange, violet, gray white, blue, yellow, and red, respectively. (b) Schematic illustration of jarosite nanosheets (KNSs and NNSs) prepared by a template-engaged redox coprecipitation method at room temperature. (c) SEM and (d) TEM images of δ-MnO_2 nanosheets. (e) SEM, (f) TEM, (g) high-magnification TEM, and (h) HRTEM images of KNSs.

prepare various 2D nanostructured electrodes with improved Li-storage properties, such as metal oxides,[31,32] metal sulfides,[33−35] lithium metal oxides,[36] the simple polyanionic compound $LiFePO_4$,[37] etc. However, the fabrication of 2D nanostructures with complex polyanionic compounds still remains very challenging.

Herein, we fabricate K-jarosite nanosheets (KNSs) and their analogues (Na-jarosite nanosheets, NNSs) via a facile template-engaged redox coprecipitation method at room temperature and employ these 2D materials as anodes for LIBs. The materials exhibit excellent Li-storage properties in terms of high capacity, superior rate capability, and ultralong cycle life. We also investigated the Li-storage mechanism of KNSs by ex situ X-ray diffraction (XRD) and X-ray photoelectron spectra (XPS) and found that the materials undergo conversion reactions at a cutoff voltage range of 0.005−3.0 V. The high specific capacities of KNS electrodes are mainly due to the synergistic function of iron oxides and oxyhydroxides with sulfates generated upon lithiation. Moreover, the as-prepared nanosheets maintain good structural integrity upon cycling and yolk−shell nanobuilding blocks simultaneously form in the 2D nanoarchitectures, which both contribute to excellent Li-storage performance.

2. EXPERIMENTAL SECTION

2.1. Materials Synthesis. First, δ-MnO_2 nanosheets are prepared by a reflux reaction between $KMnO_4$ and ethyl acetate.[38] The as-synthesized δ-MnO_2 nanosheet suspension was used as precursor for the synthesis of KNSs and NNSs. In a typical synthesis, ferrous sulfate (4.5 mmol) and potassium nitrate (1.5 mmol) were dissolved in deionized water (30 mL). Then, the obtained mixed solution was dropwise added into the above suspension of δ-MnO_2 nanosheets (50 mL; the volume ratio of deionized water/ethanol is 1:4) under magnetic stirring at room temperature. After about 10 min, an orange suspension was obtained. After aging 12 h at room temperature, the obtained suspension was centrifuged and washed by deionized water and ethanol at least three times. Finally, the orange slurry was dried under vacuum at room temperature. As for the synthesis of NNSs, it is similar to KNSs except for the use of sodium chloride as sodium source. For comparison, bulk $KFe_3(SO_4)_2(OH)_6$ was also prepared as in reference 25. In a typical synthesis, 3.0 g of potassium nitrate and 3.5 g of iron sulfate were dissolved in aqueous H_2SO_4 solution (0.01 M, 100 mL) under magnetic stirring. Then, the above mixed solution was stirred at 90 °C for 3 h. The obtained suspension was centrifuged and washed by deionized water and ethanol at least three times. Finally, the light-orange slurry was dried at 100 °C.

2.2. Characterization of Materials. The crystalline structures of the prepared products were identified by XRD (PANalytical X'pert Pro using Cu Ka radiation). The morphology of the product was observed by field-emission scanning electron microscopy (SEM, Zeiss Merlin, 1 kV), transmission electron microscopy (TEM, Zeiss 912 Omega, 120 kV), and high-resolution TEM (HRTEM, JEOL 4000 FX, 400 kV). Inductively coupled plasma-atomic emission spectrometry (ICP-AES) was performed using Spectro analytical instruments. XPS analyses were performed using an Axis Ultra instrument (Kratos Analytical Ltd., U.K.).

2.3. Electrochemical Characterization. The electrochemical properties of the products were measured using CR2032 coin-type cells with lithium metal as the negative electrode. The slurry was prepared by mixing as-prepared active materials, carbon black (super P), and sodium carboxymethyl cellulose (CMC) in a weight ratio of

DOI: 10.1021/acsami.5b01992
ACS Appl. Mater. Interfaces 2015, 7, 10518−10524

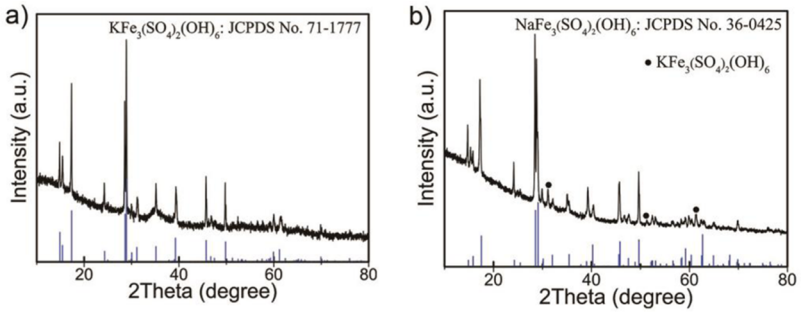

Figure 2. XRD patterns of (a) KNSs and (b) NNSs; the dot in b denotes the presence of a little amount of K-jarosite phase.

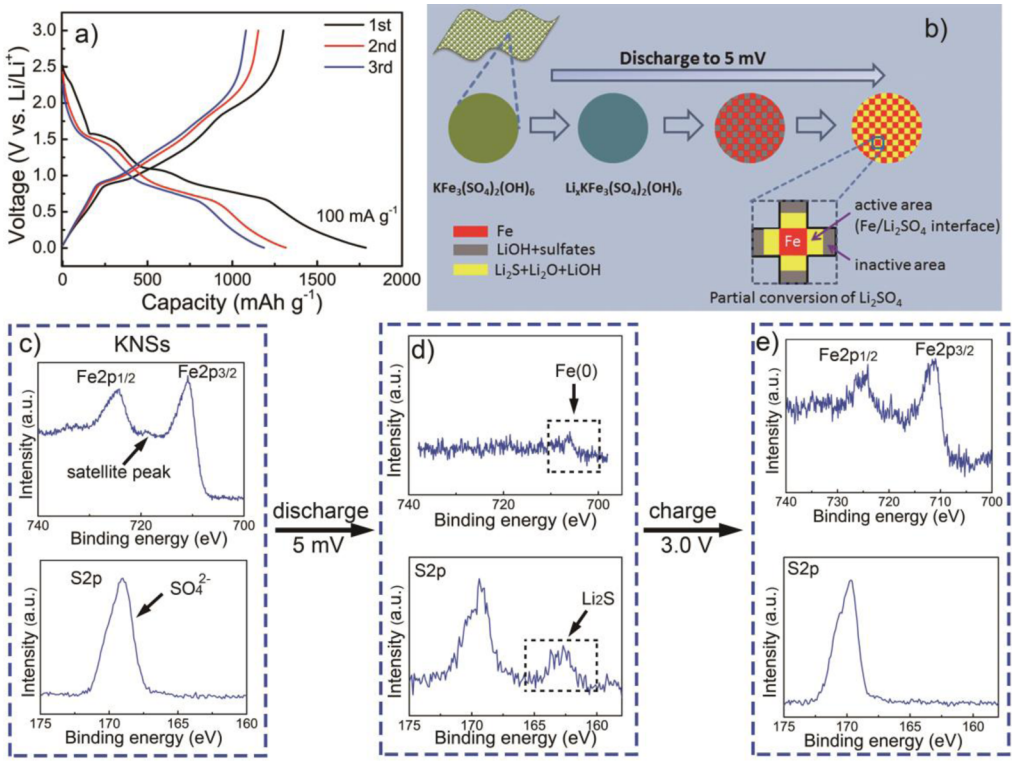

Figure 3. (a) Discharge and charge profiles of KNSs at 100 mA g^{-1} between 0.005 and 3.0 V. (b) Schematic diagram of phase evolution during the initial discharge process for KNSs electrode from open circuit potential to 5 mV. XPS spectra of KNSs for (c) pristine KNSs, (d) the discharged state, and (e) the charged state.

active material/super P/CMC = 70:20:10 in deionized water. Then, the as-prepared slurry was cast onto a copper foil current collector and dried at 60 °C overnight in a vacuum oven. The loading mass of electrode materials was 1.2−1.5 mg cm^{-2}. Cell assembly was carried out in an Ar-filled glovebox. The electrolyte solution was 1 M $LiPF_6$ in ethylene carbonate (EC)/diethyl carbonate (DEC) (1:1 v/v). Glass fiber was used as the separator. Galvanostatic charge/discharge tests were performed at room temperature using a BTS battery tester (Neware). The cutoff voltage window is 0.005−3.0 V.

3. RESULTS AND DISCUSSION

Figure 1b illustrates the fabrication of KNSs and NNSs based on a facile template-engaged redox coprecipitation method at room temperature. δ-MnO_2 nanosheets are used as both oxidant and template. A mixed aqueous solution of ferrous sulfate and potassium nitrate or sodium chloride was added dropwise to the brown suspension of δ-MnO_2 nanosheets under magnetic stirring. After around 10 min, an orange suspension is obtained, indicating the conversion of δ-MnO_2 nanosheets to KNSs or NNSs. The possible reaction mechanism is as follows. First, under the attack of Fe^{2+}, δ-MnO_2 would capture electrons from Fe^{2+} ions and simultaneously be reduced to soluble Mn^{2+} (eq 3). The generated Fe^{3+} ions would adsorb on the surface of δ-MnO_2 nanosheets. Second, Fe^{3+} will further react with SO_4^{2-} and K^+ or Na^+ by a coprecipitation reaction (eq 4), as illustrated in Figure 1b.

$$\text{Half reaction: } MnO_2 + 4H^+ + 2e^- \rightarrow Mn^{2+} + 2H_2O \quad E^{\ominus} = 1.23\ \text{V} \tag{1}$$

$$\text{Half reaction: } Fe^{3+} + e^- \rightarrow Fe^{2+} \quad E^{\ominus} = 0.77\ \text{V} \tag{2}$$

$$\text{Step 1: } MnO_2 + 2Fe^{2+} + 4H^+ \rightarrow Mn^{2+} + 2Fe^{3+} + 2H_2O \tag{3}$$

$$\text{Step 2: } K^+ + 3Fe^{3+} + 2SO_4^{2-} + 6H_2O \rightarrow KFe_3(SO_4)_2(OH)_6 + 6H^+ \tag{4}$$

DOI: 10.1021/acsami.5b01992
ACS Appl. Mater. Interfaces 2015, 7, 10518−10524

As confirmed by XRD pattern (Figure 2a), the resulting KNSs can be indexed well to rhombohedral phase jarosite $KFe_3(SO_4)_2(OH)_6$ (International Centre for Diffraction Data Powder Diffraction File (ICDD PDF) No. 71-1777). XPS measurement further confirms that Fe only exists in the form of Fe^{3+}, owing to the presence of the characteristic peak of Fe^{3+} at 719.1 eV together with two Fe 2p peaks at 711.0 and 724.4 eV (Figure 3c).[35] The Mn 2p feature peaks at 642.9 and 654.4 eV are not observed in the XPS spectra (Figure S1, Supporting Information),[38] implying the complete consumption of δ-MnO_2. This is further confirmed by ICP-AES results, which show that the weight ratio of K/Fe/S in KNSs is 7.78:31.4:12.7, revealing a potassium-rich phase of $K_{1.06}Fe_3(SO_4)_{2.11}(OH)_{5.84}$. Figure 1e,f displays typical SEM and TEM images of KNSs. The as-prepared KNSs inherit well the morphology of δ-MnO_2 nanosheets, except for a little increase of the thickness (~13 nm) compared to δ-MnO_2 nanosheets (~8.5 nm, Figure 1c,d) and that the KNS surface becomes rather rough. The high-magnification TEM image in Figure 1g shows that KNSs consist of ultrafine nanobuilding blocks of 5−10 nm. Figure 1h displays lattice fringes of HRTEM image that can be assigned to the (024) lattice-plane spacing of $KFe_3(SO_4)_2(OH)_6$. To examine the generality of the proposed synthesis method for 2D polyanionic nanostructures, we also successfully prepared 2D nanostructures of Na-jarosite, as shown in Figure S2 (Supporting Information). As displayed in Figure 2b, XRD diffraction peaks of NNSs are mainly indexed to Na-jarosite phase $NaFe_3(SO_4)_2(OH)_6$ (ICDD PDF No. 36-0425), except for the presence of a small amount of K-jarosite phase (Figure 2b). This is mainly due to the presence of a small amount of K in δ-MnO_2 prepared by the reaction between $KMnO_4$ and ethyl acetate, which is confirmed by ICP results (the weight ratio of K/Mn in δ-MnO_2 is 5.75:54.90), suggesting a possible $K_{0.14}MnO_2$ phase.

The formation of well-defined 2D nanoarchitectures would promise a superior Li-storage capability. Figure 3a shows the typical galvanostatic discharge (lithiation) and charge (delithiation) curves of KNSs between 0.005 and 3.0 V at a current density of 100 mA g^{-1}. For comparison, micrometer-sized $KFe_3(SO_4)_2(OH)_6$ was also prepared (Figure S3, Supporting Information). The first discharge and charge capacities of KNSs are 1786.7 and 1300.8 mAh g^{-1}, respectively, much higher than those of bulk sample (1553.4 and 1147.0 mAh g^{-1}; Figure S4, Supporting Information). Both KNSs and bulk sample exhibit a first Coulombic efficiency (CE) of 73%. During the subsequent two cycles, CEs of KNS electrodes promptly increased to 87 and 91%, respectively, and afterward gradually stabilized to >99.5%. The initial capacity loss can be ascribed to the irreversible lithium loss, owing to the formation of a solid electrolyte interface (SEI) layer and other Li-consuming reactions during the initial cycling.[39,40] Thus, it is demonstrated that KNSs as anode materials exhibit superior Li-storage reversibility.

The theoretical capacity of K-jarosite is 481 mAh g^{-1} (9 Li uptake), if it this estimation is just on the basis of the complete reduction of Fe^{3+} to Fe^0. However, both KNSs and bulk sample deliver reversible capacities exceeding 1000 mAh g^{-1}, more than twice as high as than the theoretical value. To investigate the extra capacity, we performed ex situ XRD and XPS measurements at different states of discharge/charge. When discharged to 1.5 V (Figure S5, Supporting Information), $KFe_3(SO_4)_2(OH)_6$ phase is well-retained except that the XRD peaks shift toward lower angles, implying the increase of lattice constants owing to Li insertion corresponding to the formation of $Li_xKFe_3(SO_4)_2(OH)_6$ ($x \leq 3.7$). With continuous discharging to 1.0, 0.6, and 0.005 V, the $Li_xKFe_3(SO_4)_2(OH)_6$ phase disappears, and the LiOH phase appears. When recharged to 3.0 V, the LiOH phase gradually disappears, and new phases (FeOOH, γ-Fe_2O_3, Li_2SO_4, and $LiKSO_4$) emerge, indicating that KNSs undergo an irreversible conversion reaction during the first cycle similar to previously reported complex oxides anodes.[41,42] Although the first lithiation for $KFe_3(SO_4)_2(OH)_6$ is irreversible, this process is probably very important because in situ generation of nanoscaled Fe and Li_2S can provide a homogeneous mixing phase, as illustrated in Figure 3b, which is beneficial to subsequent conversion reaction and interface storage process. Despite the complicated phase evolution occurring during the first cycling, the products FeOOH, γ-Fe_2O_3, Li_2SO_4, and $LiKSO_4$ can be well-retained even after 320 cycles. To further investigate the phase evolution, we also carried out XPS measurements. On discharge to 5 mV, the feature peaks of Fe^{3+} disappear, and a small peak at 706 eV emerges (Figure 3d), revealing the formation of metal Fe^0.[33] When recharged to 3.0 V, the characteristic peaks of Fe^{3+} emerge again (Figure 3e), indicating reoxidation of metal Fe^0. In addition to the valence change of Fe, a broad peak at 162.2 eV, which is assigned to Li_2S,[34,43] was also observed (Figure 3d), indicating lithiation of sulfates (such as Li_2SO_4) via a conversion reaction. Meanwhile, the peak at 169.0 eV ascribed to SO_4^{2-} still exists at the end of discharge,[34,43] manifesting partial conversion of sulfates owing to limited contacts of sulfates with metal Fe, as illustrated in Figure 3b. Li_2SO_4 is not a perceptible electronic conductor; thus, the Li-storage performance is strongly dependent on the effective contact with an electronically conductive phase such as Fe. When recharged to 3.0 V (Figure 3e), the Li_2S peak disappears, indicating reversible Li-storage of the sulfates, which is clearly demonstrated by lithiating commercial Li_2SO_4. (Detailed discussion is given in Supporting Information.) These results show the synergistic interplay of iron oxides, oxyhydroxides, and sulfates. The conversion reaction of Li_2SO_4 to Li_2S involves an eight-electron transfer, corresponding to a theoretical capacity of 1948 mAh g^{-1} (eq 7). Thus, the theoretical capacity for KNSs is 2429 mAh g^{-1} on the basis of the total conversion of $KFe_3(SO_4)_2(OH)_6$ to Fe and Li_2S. The initial discharge processes for $KFe_3(SO_4)_2(OH)_6$ are suggested to be

$$KFe_3(SO_4)_2(OH)_6 + xLi^+ + xe^- \rightarrow Li_xKFe_3(SO_4)_2(OH)_6 \quad (x \leq 3.7) \tag{5}$$

$$Li_xKFe_3(SO_4)_2(OH)_6 + (9-x)Li^+ + (9-x)e^- \rightarrow 3Fe + Li_2SO_4 + LiKSO_4 + 6LiOH \tag{6}$$

$$Li_2SO_4 + 8Li^+ + 8e^- \rightarrow Li_2S + 4Li_2O \tag{7}$$

During the subsequent charge process, the reversible reactions would be the reoxidation of in situ produced metal Fe and Li_2S in the Li_2O and LiOH matrix, respectively.

$$Fe + LiOH + Li_2O \leftrightarrow FeOOH + 3Li^+ + 3e^- \tag{8}$$

$$Fe + 3/2Li_2O \leftrightarrow 1/2Fe_2O_3 + 3Li^+ + 3e^- \tag{9}$$

$$Li_2S + 4Li_2O \leftrightarrow Li_2SO_4 + 8Li^+ + 8e^- \tag{10}$$

DOI: 10.1021/acsami.5b01992
ACS Appl. Mater. Interfaces 2015, 7, 10518−10524

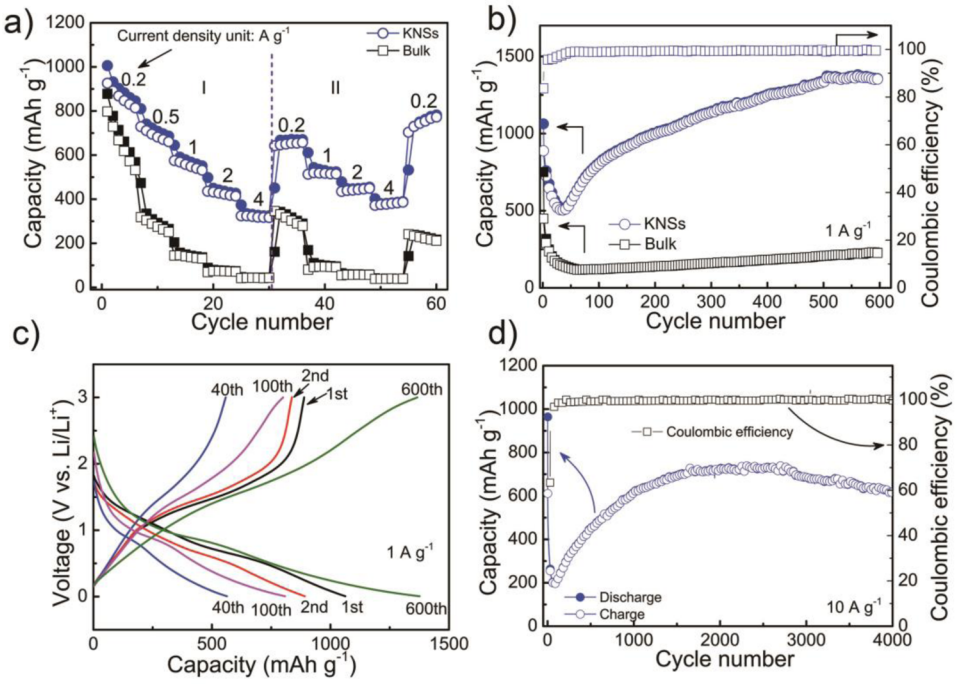

Figure 4. (a) Rate capabilities of KNSs from 0.2 to 4 A g^{-1}. (b) Cycling performance of KNSs at the current densities of 1 A g^{-1}. (c) Discharge and charge curves of KNSs under different cycles at 1 A g^{-1}. (d) Long-term cycling performance of KNSs at 10 A g^{-1}.

Besides the obtained high capacity for KNSs, the materials exhibit superior rate capability as well. On increasing current densities from 200 to 1000, 2000, and 4000 mA g^{-1} (part II in Figure 4a), KNSs deliver reversible capacities of 670, 530, 450, and 380 mAh g^{-1}, respectively, which are 2−10 times higher than those of the bulk counterpart (317, 93, 57, and 38 mAh g^{-1}). When the current density is reduced back to 200 mA g^{-1}, a reversible capacity of above 750 mAh g^{-1} was maintained. Both KNSs and bulk sample undergo fast capacity decay during the initial 40 cycles and then exhibit a gradually capacity increase (Figures 4a and S7). This is clearly observed in the charge/discharge profiles at different cycles (Figure 4c). The initial capacity decay is mainly due to low Li^+ diffusion and large Li^+ charge-transfer resistance. On increasing cycles, nanosized Fe would be gradually produced on a large scale, which can improve Li^+ diffusion dynamics,[45] as confirmed by our CV tests for different cycles in Figure S8 (Supporting Information). The capacity rise could be attributed to the following aspects: (i) The decreased cell resistance and enhanced Li^+ dynamics after initial activation process are probably beneficial to improving the electrochemical performance. This phenomenon is also observed for Fe_2O_3 and CuO materials,[45] revealing that the cell resistance after cycles becomes smaller than those of the cell before cycling, as based on the impedance result. (ii) On increasing cycles, the formed organic/inorganic layer on the surface of active particles provides additional reversible Li storage as well.[48] (iii) The effects of electrochemical milling can reduce the particle size, which also facilitates Li^+ storage.[45] In addition, more Fe/Li_2O contacts formed after the activation process would also promote more interfacial Li^+ storage,[3,44] leading to capacity increasing upon cycling. Despite this, the as-prepared materials still deliver excellent long-term cyclability. As shown in Figure 4b, a specific capacity as high as 1350 mAh g^{-1} can be attained after 600 cycles at 1 A g^{-1}, which is almost six times higher than that of bulk sample (226 mAh g^{-1}). Even at a very high current density of 10 A g^{-1}, a reversible capacity of 620 mAh g^{-1} can be retained after 4000 cycles (Figure 4d). This cycling performance and high rate capability are distinctly better than those reported for comparable Fe-based compounds.[41,46,47] To investigate the generality of the application potential of the materials belonging to the jarosite family compounds as anodes, we also evaluated the Li-storage behaviors of NNSs, which deliver excellent Li-storage performance as well (Figure S9, Supporting Information).

To examine the stability of the obtained 2D nanoarchitectures upon cycling, SEM, TEM, and HRTEM were performed on the cycled electrode. Figure 5a shows that the nanosheet structures are mainly preserved after 100 cycles at 500 mA g^{-1}. Figure 5b,c shows that the surface of the nanobuilding blocks in KNSs is covered by a uniform protection layer (thickness ≈ 5 nm). Interestingly, most of the nanobuilding blocks (marked by arrows in Figure 5b) convert to yolk−shell structures, probably resulting from the irreversible volume changes upon cycling. Fourier transforms (FTs) in Figure 5c indicate that the shell layer is composed of amorphous and crystalline components, which might be due to the combination formation of conversion reaction materials together with SEI layer,[48−50] thus forming a hybrid shell layer. The resulting yolk−shell structure could be beneficial to improving the cycling stability of KNSs because it can not only effectively protect the core from the electrolyte corrosion but also accommodate the volume changes caused by repeated Li^+ insertion/extraction processes, as illustrated in Figure 5d.[51,52]

4. CONCLUSIONS

We report the fabrication of 2D nanostructures of K-jarosite and its analogues by a facile template-engaged redox coprecipitation at room temperature and demonstrate their feasibilities as anode materials for LIBs for the first time. The as-prepared materials exhibit high capacity, excellent rate capability, and ultralong cycle life. The reversible Li storage

DOI: 10.1021/acsami.5b01992
ACS Appl. Mater. Interfaces 2015, 7, 10518−10524

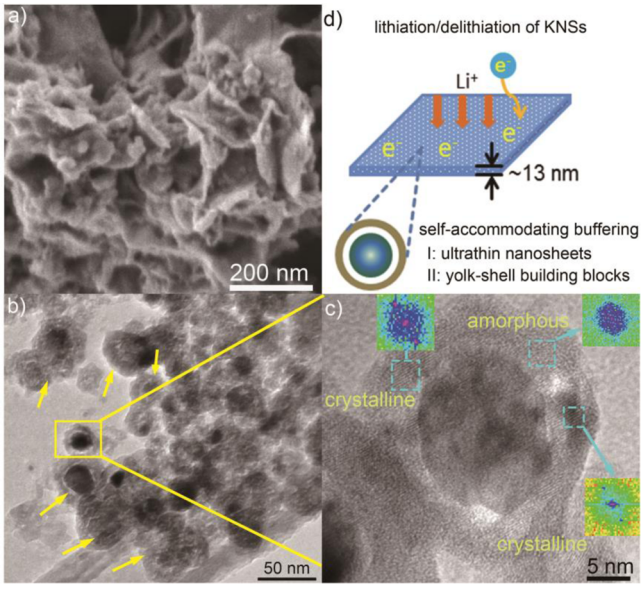

Figure 5. (a) SEM and (b) TEM images of KNSs electrodes after 100 cycles at 500 mA g^{-1}. (c) Magnified view taken from boxed area in b; the insets show FTs corresponding to the boxed areas. (d) Schematic illustration of the lithiation/delithiation process for KNSs electrode.

of these 2D materials is based on the synergistic conversion reactions of iron oxides and oxyhydroxides and sulfates. Moreover, not only can the 2D nanoassemblies be well-retained upon cycling, but also can yolk–shell nanobuilding blocks form simultaneously in the whole nanoarchitecture, both of which are important for the remarkable Li-storage properties. Such findings have important implications for the large-scale application of Fe-based polyanionic materials as environmentally friendly, low-cost, and earth-abundant anode materials for long-life LIBs.

■ ASSOCIATED CONTENT

Supporting Information

SEM images of NNSs and bulk K-jarosite; the charge and discharge profiles of bulk K-jarosite; ex situ XRD patterns of KNSs; the charge and discharge curves of bulk Fe_2O_3, Fe_2O_3/Li_2SO_4 composites, and Li_2SO_4/super P composite; the schematic diagrams of lithiation process of Fe_2O_3/Li_2SO_4 bulk composites, Fe_2O_3/Li_2SO_4 nanocomposites, and KNSs; the capacity ratios between KNSs and bulk sample as a function of current densities; CV curves of KNSs electrode for different cycles; the charge and discharge profiles and cycling performance of NNSs; XPS spectrum of KNSs. The Supporting Information is available free of charge on the ACS Publications website at DOI: 10.1021/acsami.5b01992.

■ AUTHOR INFORMATION

Corresponding Author

*E-mail: yanyumse@ustc.edu.cn.

Notes

The authors declare no competing financial interest.

■ ACKNOWLEDGMENTS

We thank Mr. Mitsuharu Konuma for XPS measurement and Dr. H. Hoier for XRD measurements. This work was financially supported by the Alexander von Humboldt Foundation (Sofja Kovalevskaja award), the National Natural Science Foundation of China (nos. 21171015 and 21373195), the Recruitment Program of Global Experts, the program for New Century Excellent Talents in University (NCET-12-0515), the Fundamental Research Funds for the Central Universities (WK2060140014 and WK2060140016), the Collaborative Innovation Center of Suzhou Nano Science and Technology, and the Max Planck Society as well as the European Union Seventh Framework Programme (FP7/2007-2013) under grant agreement no. 312483 (ESTEEM2).

■ REFERENCES

(1) Dunn, B.; Kamath, H.; Tarascon, J.-M. Electrical Energy Storage for the Grid: a Battery of Choices. *Science* **2011**, *334*, 928–935.
(2) Barpanda, P.; Ati, M.; Melot, B. C.; Rousse, G.; Chotard, J.-N.; Doublet, M.-L.; Sougrati, M. T.; Corr, S.; Jumas, J.-C.; Tarascon, J.-M. A 3.90 V Iron-Based Fluorosulphate Material for Lithium-Ion Batteries Crystallizing in the Triplite Structure. *Nat. Mater.* **2011**, *10*, 772–779.
(3) Maier, J. Thermodynamics of Electrochemical Lithium Storage. *Angew. Chem., Int. Ed.* **2013**, *52*, 4998–5026.
(4) Yu, Y.; Gu, L.; Wang, C.; Dhanabalan, A.; van Aken, P. A.; Maier, J. Encapsulation of Sn@Carbon Nanoparticles in Bamboo-Like Hollow Carbon Nanofibers as an Anode Material in Lithium-Based Batteries. *Angew. Chem., Int. Ed.* **2009**, *48*, 6485–6489.
(5) Yu, Y.; Yan, C.; Gu, L.; Lang, X.; Tang, K.; Zhang, L.; Hou, Y.; Wang, Z.; Chen, M. W.; Schmidt, O. G. Three-Dimensional (3D) Bicontinuous Au/Amorphous-Ge Thin Films as Fast and High-Capacity Anodes for Lithium-Ion Batteries. *Adv. Energy Mater.* **2013**, *3*, 281–285.
(6) Xu, C.; Zeng, Y.; Rui, X. H.; Xiao, N.; Zhu, J. X.; Zhang, W. Y.; Chen, J.; Liu, W. L.; Tan, H. T.; Hng, H. H.; Yan, Q. Y. Controlled Soft-Template Synthesis of Ultrathin C@FeS Nanosheets with High-Li-Storage Performance. *ACS Nano* **2012**, *6*, 4713–4721.
(7) Reddy, M.; Yu, T.; Sow, C.-H.; Shen, Z. X.; Lim, C. T.; Subba Rao, G.; Chowdari, B. α-Fe_2O_3 Nanoflakes as an Anode Material for Li-Ion Batteries. *Adv. Funct. Mater.* **2007**, *17*, 2792–2799.
(8) Wang, H.; Cui, L.-F.; Yang, Y.; Sanchez Casalongue, H.; Robinson, J. T.; Liang, Y.; Cui, Y.; Dai, H. Mn_3O_4-Graphene Hybrid as a High-Capacity Anode Material for Lithium Ion Batteries. *J. Am. Chem. Soc.* **2010**, *132*, 13978–13980.
(9) Ding, Y.-L.; Wen, Y.; Van Aken, P. A.; Maier, J.; Yu, Y. Large-Scale Low Temperature Fabrication of SnO_2 Hollow/Nanoporous Nanostructures: the Template-Engaged Replacement Reaction Mechanism and High-Rate Lithium Storage. *Nanoscale* **2014**, *6*, 11411–11418.
(10) Yu, Y.; Gu, L.; Zhu, C.; van Aken, P. A.; Maier, J. Tin Nanoparticles Encapsulated in Porous Multichannel Carbon Microtubes: Preparation by Single-Nozzle Electrospinning and Application as Anode Material for High-Performance Li-Based Batteries. *J. Am. Chem. Soc.* **2009**, *131*, 15984–15985.
(11) Yu, Y.; Gu, L.; Zhu, C.; Tsukimoto, S.; van Aken, P. A.; Maier, J. Reversible Storage of Lithium in Silver-Coated Three-Dimensional Macroporous Silicon. *Adv. Mater.* **2010**, *22*, 2247–2250.
(12) Hu, Y. S.; Demir-Cakan, R.; Titirici, M. M.; Müller, J. O.; Schlögl, R.; Antonietti, M.; Maier, J. Superior Storage Performance of a Si@SiO_x/C Nanocomposite as Anode Material for Lithium-Ion Batteries. *Angew. Chem., Int. Ed.* **2008**, *47*, 1645–1649.
(13) Wang, L.; He, X.; Li, J.; Sun, W.; Gao, J.; Guo, J.; Jiang, C. Nano-Structured Phosphorus Composite as High-Capacity Anode Materials for Lithium Batteries. *Angew. Chem., Int. Ed.* **2012**, *51*, 9034–9037.
(14) Chen, J.; Xu, L.-N.; Li, W.-Y.; Gou, X.-L. α-Fe_2O_3 Nanotubes in Gas Sensor and Lithium-Ion Battery Applications. *Adv. Mater.* **2005**, *17*, 582–586.
(15) Taberna, P.-L.; Mitra, S.; Poizot, P.; Simon, P.; Tarascon, J.-M. High Rate Capabilities Fe_3O_4-Based Cu Nano-Architectured Electrodes for Lithium-Ion Battery Applications. *Nat. Mater.* **2006**, *5*, 567–573.

DOI: 10.1021/acsami.5b01992
ACS Appl. Mater. Interfaces 2015, 7, 10518–10524

(16) Su, L. W.; Zhou, Z.; Shen, P. W. Core-shell Fe@Fe_3C/C Nanocomposites as Anode Materials for Li Ion Batteries. *Electrochim. Acta* **2013**, *87*, 180−185.
(17) Boyanov, S.; Bernardi, J.; Gillot, F.; Dupont, L.; Womes, M.; Tarascon, J. M.; Monconduit, L.; Doublet, M. L. FeP: Another Attractive Anode for the Li-Ion Battery Enlisting a Reversible Two-Step Insertion/Conversion Process. *Chem. Mater.* **2006**, *18*, 3531−3538.
(18) Boyanov, S.; Womes, M.; Monconduit, L.; Zitoun, D. Mossbauer Spectroscopy and Magnetic Measurements As Complementary Techniques for the Phase Analysis of FeP Electrodes Cycling in Li-Ion Batteries. *Chem. Mater.* **2009**, *21*, 3684−3692.
(19) Bresser, D.; Paillard, E.; Kloepsch, R.; Krueger, S.; Fiedler, M.; Schmitz, R.; Baither, D.; Winter, M.; Passerini, S. Carbon Coated $ZnFe_2O_4$ Nanoparticles for Advanced Lithium-Ion Anodes. *Adv. Energy Mater.* **2013**, *3*, 513−523.
(20) Bomio, M.; Lavela, P.; Tirado, J. Electrochemical Evaluation of $CuFe_2O_4$ Samples Obtained by Sol−Gel Methods Used as Anodes in Lithium Batteries. *J. Solid State Electrochem.* **2008**, *12*, 729−737.
(21) Zhao, H.; Zheng, Z.; Wong, K. W.; Wang, S.; Huang, B.; Li, D. Fabrication and Electrochemical Performance of Nickel Ferrite Nanoparticles as Anode Material in Lithium Ion Batteries. *Electrochem. Commun.* **2007**, *9*, 2606−2610.
(22) Lavela, P.; Tirado, J. L. $CoFe_2O_4$ and $NiFe_2O_4$ Synthesized by Sol-Gel Procedures for Their Use as Anode Materials for Li Ion Batteries. *J. Power Sources* **2007**, *172*, 379−387.
(23) Subban, C. V.; Ati, M.; Rousse, G.; Abakumov, A. M.; Van Tendeloo, G.; Janot, R. l.; Tarascon, J.-M. Preparation, Structure, and Electrochemistry of Layered Polyanionic Hydroxysulfates: $LiMSO_4OH$ (M = Fe, Co, Mn) Electrodes for Li-Ion Batteries. *J. Am. Chem. Soc.* **2013**, *135*, 3653−3661.
(24) Gnanavel, M.; Pralong, V.; Lebedev, O. I.; Caignaert, V.; Bazin, P.; Raveau, B. Lithium Intercalation into the Jarosite-type Hydroxysulfate: A Topotactic Reversible Reaction from a Crystalline Phase to an Inorganic Polymer-like Structure. *Chem. Mater.* **2014**, *26*, 4521−4527.
(25) Dutrizac, J.; Kaiman, S. Synthesis and Properties of Jarosite-Type Compounds. *Can. Mineral.* **1976**, *14*, 151−158.
(26) Smith, A. M.; Hudson-Edwards, K. A.; Dubbin, W. E.; Wright, K. Dissolution of Jarosite $KFe_3(SO_4)_2(OH)_6$ at pH 2 and 8: Insights from Batch Experiments and Computational Modelling. *Geochim. Cosmochim. Acta* **2006**, *70*, 608−621.
(27) Madden, M. E.; Bodnar, R.; Rimstidt, J. Jarosite as an Indicator of Water-Limited Chemical Weathering on Mars. *Nature* **2004**, *431*, 821−823.
(28) Fujita, T.; Yamaguchi, H.; Kimura, S.; Kashiwagi, T.; Hagiwara, M.; Matan, K.; Grohol, D.; Nocera, D.; Lee, Y. High-Field Multifrequency ESR in the S = $^5/_2$ Kagome-Lattice Antiferromagnet $KFe_3(OH)_6$ $(SO_4)_2$. *Phys. Rev. B* **2012**, *85*, 094409.
(29) Grohol, D.; Matan, K.; Cho, J.-H.; Lee, S.-H.; Lynn, J. W.; Nocera, D. G.; Lee, Y. S. Spin Chirality on a Two-Dimensional Frustrated Lattice. *Nat. Mater.* **2005**, *4*, 323−328.
(30) Wagemaker, M.; Mulder, F. M. Properties and Promises of Nanosized Insertion Materials for Li-Ion Batteries. *Acc. Chem. Res.* **2013**, *46*, 1206−1215.
(31) Kundu, M.; Ng, C. C. A.; Petrovykh, D. Y.; Liu, L. F. Nickel Foam Supported Mesoporous MnO_2 Nanosheet Arrays with Superior Lithium Storage Performance. *Chem. Commun.* **2013**, *49*, 8459−8461.
(32) Wang, X.; Wu, X. L.; Guo, Y. G.; Zhong, Y. T.; Cao, X. Q.; Ma, Y.; Yao, J. N. Synthesis and Lithium Storage Properties of Co_3O_4 Nanosheet-Assembled Multishelled Hollow Spheres. *Adv. Funct. Mater.* **2010**, *20*, 1680−1686.
(33) Zhuo, S. F.; Xu, Y.; Zhao, W. W.; Zhang, J.; Zhang, B. Hierarchical Nanosheet-Based MoS_2 Nanotubes Fabricated by an Anion-Exchange Reaction of MoO_3-Amine Hybrid Nanowires. *Angew. Chem., Int. Ed.* **2013**, *52*, 8602−8606.
(34) Han, W.; Gao, M. Investigations on Iron Sulfide Nanosheets Prepared via a Single-Source Precursor Approach. *Cryst. Growth Des.* **2008**, *8*, 1023−1030.
(35) Kim, T.-J.; Kim, C.; Son, D.; Choi, M.; Park, B. Novel SnS_2-Nanosheet Anodes for Lithium-Ion Batteries. *J. Power Sources* **2007**, *167*, 529−535.
(36) Chen, S.; Xin, Y.; Zhou, Y.; Ma, Y.; Zhou, H.; Qi, L. Self-Supported $Li_4Ti_5O_{12}$ Nanosheet Arrays for Lithium Ion Batteries with Excellent Rate Capability and Ultralong Cycle Life. *Energy Environ. Sci.* **2014**, *7*, 1924−1930.
(37) Zhao, Y.; Peng, L.; Liu, B.; Yu, G. Single-Crystalline $LiFePO_4$ Nanosheets for High-Rate Li-Ion Batteries. *Nano Lett.* **2014**, *14*, 2849−2853.
(38) Sinha, A. K.; Pradhan, M.; Pal, T. Morphological Evolution of Two-Dimensional MnO_2 Nanosheets and Their Shape Transformation to One-Dimensional Ultralong MnO_2 Nanowires for Robust Catalytic Activity. *J. Phys. Chem. C* **2013**, *117*, 23976−23986.
(39) Valvo, M.; Lindgren, F.; Lafont, U.; Björefors, F.; Edström, K. Towards More Sustainable Negative Electrodes in Na-Ion Batteries via Nanostructured Iron Oxide. *J. Power Sources* **2014**, *245*, 967−978.
(40) Larcher, D.; Masquelier, C.; Bonnin, D.; Chabre, Y.; Masson, V.; Leriche, J.-B.; Tarascon, J.-M. Effect of Particle Size on Lithium Intercalation into α-Fe_2O_3. *J. Electrochem. Soc.* **2003**, *150*, A133−A139.
(41) Reddy, M.; Subba Rao, G.; Chowdari, B. Metal Oxides and Oxysalts as Anode Materials for Li Ion Batteries. *Chem. Rev.* **2013**, *113*, 5364−5457.
(42) Su, Q.; Xie, D.; Zhang, J.; Du, G.; Xu, B. In Situ Transmission Electron Microscopy Observation of the Conversion Mechanism of Fe_2O_3/Graphene Anode during Lithiation−Delithiation Processes. *ACS Nano* **2013**, *7*, 9115−9121.
(43) Feng, X.; Song, M.-K.; Stolte, W. C.; Gardenghi, D.; Zhang, D.; Sun, X.; Zhu, J.; Cairns, E. J.; Guo, J. Understanding the Degradation Mechanism of Rechargeable Lithium/Sulfur Cells: a Comprehensive Study of the Sulfur−Graphene Oxide Cathode after Discharge−Charge Cycling. *Phys. Chem. Chem. Phys.* **2014**, *16*, 16931−16940.
(44) Fu, L.; Chen, C.-C.; Samuelis, D.; Maier, J. Thermodynamics of Lithium Storage at Abrupt Junctions: Modeling and Experimental Evidence. *Phys. Rev. Lett.* **2014**, *112*, 208301.
(45) Hassan, M. F.; Guo, Z.; Chen, Z.; Liu, H. α-Fe_2O_3 as an Anode Material with Capacity Rise and High Rate Capability for Lithium-Ion Batteries. *Mater. Res. Bull.* **2011**, *46*, 858−864.
(46) Lin, Y.-M.; Abel, P. R.; Heller, A.; Mullins, C. B. α-Fe_2O_3 Nanorods as Anode Material for Lithium Ion Batteries. *J. Phys. Chem. Lett.* **2011**, *2*, 2885−2891.
(47) Cheng, F.; Tao, Z.; Liang, J.; Chen, J. Template-Directed Materials for Rechargeable Lithium-Ion Batteries. *Chem. Mater.* **2008**, *20*, 667−681.
(48) Su, L.; Zhong, Y.; Zhou, Z. Role of Transition Metal Nanoparticles in the Extra Lithium Storage Capacity of Transition Metal Oxides: a Case Study of Hierarchical Core−Shell Fe_3O_4@C and Fe@C Microspheres. *J. Mater. Chem. A* **2013**, *1*, 15158−15166.
(49) Aurbach, D. Review of Selected Electrode−Solution Interactions Which Determine the Performance of Li and Li Ion Batteries. *J. Power Sources* **2000**, *89*, 206−218.
(50) Zhang, S.; Ding, M. S.; Xu, K.; Allen, J.; Jow, T. R. Understanding Solid Electrolyte Interface Film Formation on Graphite Electrodes. *Electrochem. Solid-State Lett.* **2001**, *4*, A206−A208.
(51) Seh, Z. W.; Li, W. Y.; Cha, J. J.; Zheng, G. Y.; Yang, Y.; McDowell, M. T.; Hsu, P. C.; Cui, Y. Sulphur-TiO_2 Yolk-Shell Nanoarchitecture with Internal Void Space for Long-Cycle Lithium-Sulphur Batteries. *Nat. Commun.* **2013**, *4*, 1331.
(52) Cui, Z. M.; Chen, Z.; Cao, C. Y.; Jiang, L.; Song, W. G. A Yolk-Shell Structured Fe_2O_3@Mesoporous SiO_2 Nanoreactor for Enhanced Activity as a Fenton Catalyst in Total Oxidation of Dyes. *Chem. Commun.* **2013**, *49*, 2332−2334.

DOI: 10.1021/acsami.5b01992
ACS Appl. Mater. Interfaces 2015, 7, 10518−10524